Photon-counting X-ray CT perfusion imaging in animal models of cancer

Darin P. Clark,[a] Alex J. Allphin,[a] Yvonne M. Mowery,[b] and Cristian T. Badea[a*]

[a]Quantitative Imaging and Analysis Lab, Duke University, Dept. of Radiology, Durham, NC 27710
[b]Duke University, Dept. of Radiation Oncology, Durham, NC 27710 USA

ABSTRACT

Photon-counting detector (PCD) CT promises to improve routine CT imaging applications with higher spatial resolution, lower levels of noise at fixed dose, and improved image contrast while providing spectral information with every scan. We propose and demonstrate a novel application of PCD imaging in a preclinical model of head and neck squamous cell carcinoma: spectral perfusion imaging of cancer. To handle the high dimensionality of our data set (3D volumes at 12 perfusion time points times 4 energy thresholds), we update our previously proposed multi-channel iterative reconstruction algorithm to handle the perfusion reconstruction problem, and we propose an extension which adds patch-based singular value thresholding (pSVT) along the perfusion dimension. Adding pSVT reduces noise by an additional 45% relative to our standard algorithm, which itself reduces noise by 2-7 times relative to analytical reconstruction. Preliminary analysis suggests that the addition of pSVT does not negatively impact material decomposition accuracy or image spatial resolution. Notable weaknesses of this preliminary study include relatively high contrast agent dose (0.5 mL *ISOVUE-370* over 10 seconds), ionizing radiation dose (~570 mGy), and computation time (2.9 hours, no pSVT; 11 hours with pSVT); however, following from our past work, our reconstruction algorithm may be an ideal source of training labels for supervised deep learning applied to computationally cheap analytical reconstructions.

Keywords: X-ray CT, photon counting, multi-energy CT, perfusion, preclinical, head and neck cancer

*cristian.badea@duke.edu; phone 1-919-684-7509; https://sites.duke.edu/qial/

1. INTRODUCTION

Photon-counting detector (PCD) technology brings significant advancements to traditional X-ray CT imaging applications, including higher spatial resolution, reduced electronic noise, and improved image contrast.[1, 2] Furthermore, replacing traditional energy-integrating detectors with PCDs in routine imaging applications will intrinsically provide spectral information for artifact reduction and post-processing. Fully exploiting this spectral information will enable novel applications of multi-contrast imaging and even functional targeting of CT contrast.[3, 4] Practically, a new generation of data processing algorithms is required to take full advantage of spectral information at current dose levels because of the increased noise associated with photon binning and multi-material decomposition.

In this work, we demonstrate a new application of PCCT, spectral perfusion imaging of cancer, as a future alternative to contrast-enhanced CT imaging protocols like those used to stage head and neck squamous cell carcinoma (HNSCC) in humans.[5] Specifically, we present a preclinical experiment using a syngeneic transplant oral cavity model of HNSCC (MOC2)[6] initiated in C57BL/6J mice by implantation of cells into the buccal mucosa. To handle high levels of noise associated with PCCT and preclinical imaging, we extend our previously proposed iterative reconstruction algorithm from spectral[7] and cardiac[8] applications to multi-channel perfusion reconstruction. New to this work we employ an updated version of our rank-sparse kernel regression (RSKR)[7] algorithm which includes localized noise estimation for handling spatial variance and patch-based singular value thresholding[9] for improved temporal redundancy.

2. MATERIALS AND METHODS

2.1 Data acquisition

Our photon counting micro-CT system uses a SANTIS 1604 detector (DECTRIS Ltd.). The detector is constructed with a 1 mm thick CdTe sensor, 150-μm isotropic pixels (1035x257), and four independent energy thresholds, here set to 20, 25, 34, and 50 keV to bracket the K-edge of iodine. The projection data set was acquired with a G297 X-ray tube (Varian Medical Systems; fs = 0.3/0.8 mm; tungsten rotating anode; filtration: 0.1 mm Cu; 80 kVp, 2.5 mA, 90 ms exposure / projection). The source-to-detector and source-to-object distances were 821 mm and 674 mm, respectively. To minimize

ring artifacts in our reconstructions, we scanned using a helical trajectory with 3 rotations (45 seconds/rotation) and 1.25 cm of total translation during scanning, acquiring a total of 1500 projections per threshold. This acquisition protocol was repeated 4 times, consecutively, yielding a total of 6000 projections over 540 seconds. The absorbed radiation dose associated with imaging was ~570 mGy. To image perfusion, we injected 0.5 ml of *ISOVUE-370* (Bracco Diagnostic Inc.) over 10 secs via a tail vein catheter using a computer-controlled injector (*Nexus 3000*; Chemyx Inc.), starting 22.5 seconds after beginning the scan.

The animal scan conducted for this work followed protocols approved by the Duke University Institutional Animal Care and Use Committee. The animal model was a syngeneic transplant oral cavity squamous cell carcinoma model (MOC2)[6] initiated in a C57BL/6J mouse by implantation of 30,000 cells into the buccal mucosa (median time to tumor onset: 2.2 weeks). The model exhibits metastasis to the cervical lymph nodes, similar to the natural history of human HNSCC. Imaging was performed when caliper measurements of the primary tumor fell in the range of 50-75 mm^3.

2.2 Reconstruction

To handle the channels of photon-counting perfusion data (3D volumes with n_x voxels, n_t time points, and n_e energy thresholds), we organize the reconstructions into a 3D array:

$$X := \begin{bmatrix} [\mathbf{X}_{t=1} & \mathbf{X}_{t=2} & \cdots & \mathbf{X}_{t=n_t}]_{e=1} \\ & \cdots & \\ [\mathbf{X}_{t=1} & \mathbf{X}_{t=2} & \cdots & \mathbf{X}_{t=n_t}]_{e=n_e} \end{bmatrix}, \tag{1}$$

where, e.g., $\mathbf{x}_{t=1,e=2}$ denotes a column vector of the reconstruction at perfusion time point 1 and energy threshold 2. Each energy threshold slice corresponds to a 2D matrix. Following from this notation (array, *A*; matrix, A; vector, **a**; scalar, a; index, *a*), algebraic reconstruction minimizes the reconstruction error relative to log-transformed projection data, **y**, under an L2 norm penalty applied separately to each channel:

$$X = \frac{\arg\min}{X} \frac{1}{2}\|RX - \mathbf{y}\|_Q^2 := \frac{\arg\min}{X} \frac{1}{2} \sum_{t=1}^{n_t} \sum_{e=1}^{n_e} \left[(R\mathbf{x}_{t,e} - \mathbf{y})^T Q_{t,e} (R\mathbf{x}_{t,e} - \mathbf{y}) \right]. \tag{2}$$

R is the system-specific projection matrix, which is universal for all channels when working with co-registered photon counting projection data. The weight array Q is constructed from weight matrices, $Q_{t,e}$, the product of diagonal matrices indicating the target energy threshold and perfusion phase.

We use multi-channel regularization to improve reconstruction performance. Specifically, we perform iterative reconstruction using the split Bregman optimization framework,[10] and we employ an extended version of our RSKR regularizer to enforce gradient sparsity and data consistency between channels.[7] Our iterative reconstruction is governed by the following objective function:

$$X = \frac{\arg\min}{X} \frac{1}{2}\|RX - \mathbf{y}\|_Q^2 + \lambda_{*1}\|X_{n_x n_t \times n_e}\|_* + \lambda_S\|X_{n_x n_t \times n_e}\|_{BTV} + \lambda_{*2} \sum_{p=1}^{n_p}\|P_p(X_{n_x n_e \times n_t})\|_*. \tag{3}$$

$X_{n_x n_t \times n_e}$ denotes the unfolding of the array X into a matrix with $n_x n_t$ rows and n_e columns ($X_{n_x n_e \times n_t}$: $n_x n_e$ rows, n_t columns). These unfoldings and their corresponding regularization terms enable penalization of the global spectral rank ($\|.\|_*$, nuclear norm; λ_{*1}), the spectrally joint intensity gradient sparsity (BTV: bilateral total variation[7]; λ_S), and the patch-wise temporal rank (λ_{*2}; n_p total patches; P_p: patch extraction operator for patch p). Within the split Bregman framework, it is feasible to split each regularization term into a separate regularization sub-step (each with its own set of auxiliary variables, D and V) to incrementally solve this objective function. Practically, however, the computational cost of the data fidelity updates (Fig. 1, step 6; here, evaluated on 48 volumes) and the often slow rate of convergence of shrinkage methods (singular value thresholding to reduce the nuclear norm[11]) make this approach intractable.

To reduce the number of global Bregman iterations (data fidelity update steps) required to achieve convergence (here, 3), we address all of the regularization terms in a single regularization step (step 4). This one step is itself solved by a series of inner Bregman iterations (3-4), which perform image-domain denoising with our RSKR algorithm (steps 4a-4i). RSKR jointly minimizes the spectral rank (λ_{*1} term) and the spectral gradient sparsity (λ_S term) by performing joint bilateral filtration on singular vectors computed along the energy dimension (step 4b). As in our previous implementations of RSKR, we use the median absolute deviation (MAD[12]) to estimate the noise level in each channel. These noise estimates are used to weight the singular value decomposition such that high singular values correspond to singular vectors with

proportionately high signal-to-noise ratios (steps 4a, 4b). As in past work, a similar noise estimation strategy is used to calibrate the joint bilateral filter parameters (jBF[7]; step 4e), reducing the number of free parameters which must be determined by the user to achieve robust performance.

New to this work, we have improved our implementation of BF to use local noise estimates (vs. one global noise estimate per energy) to deal with spatially variant noise levels in CT data. Our GPU-based implementation of jBF now computes the MAD of image gradients in 32x32 patches with a stride of 16 voxels in axial planes. Overlapping estimates are averaged to prevent sharp transitions in denoising performance, while the noise level is estimated in axial planes, rather than volumetrically, to improve computational efficiency.

Also new to this work, we perform patch-based singular value thresholding (pSVT[9]) along the time dimension of the singular vectors. Notably, pSVT is applied to the singular values of a second singular value decomposition performed on $3^3 \times n_t$ patch matrices extracted from L (step 4f). Given a vector of these singular values, $\boldsymbol{\varepsilon}$, computed from patch matrix p, thresholding is applied to the singular values (indexed by i; evaluated separately per energy) as follows:

$$\varepsilon'_{p,i,e} = \max\left(\varepsilon_{p,i,e} - \tau_{i,e}\left(\frac{\varepsilon_{p,i,e}}{\varepsilon_{p,0,e}}\right)^{\nu-1}, 0\right). \tag{4}$$

These thresholded singular values, $\boldsymbol{\varepsilon}'$, are then used to reverse the SVD for each patch matrix, and the central voxel for each time point is stored as the regularized output.

Previously, we have used kernel smoothing to overcome inconsistent denoising performance at high contrast edges when denoising with jBF.[13] Now, we apply pSVT ($\nu = 0.7$). pSVT similarly improves image consistency at edges, but also improves consistency along the time dimension and may better preserve spatial resolution. pSVT addresses the final cost term of the Objective function (Eq. 3; Fig. 1; λ_{*2}). Like with jBF, MAD-based noise estimates are used to calibrate the threshold values, $\tau_{i,e}$, used during each inner Bregman iteration. Specifically, the SVD is performed on zero-mean Gaussian noise patch matrices with noise standard deviations matching those measured globally in the corresponding energy channel. Here, the average singular values from 125 noise realizations were used to set the threshold values per energy.

Objective: $X = \underset{X}{\arg\min}\frac{1}{2}\|RX - \mathbf{y}\|_Q^2 + \lambda_{*,1}\|X_{n_x n_t \times n_e}\|_* + \lambda_S\|X_{n_x n_t \times n_e}\|_{BTV} + \lambda_{*,2}\sum_{p=1}^{n_p}\|P_p(X_{n_x n_e \times n_t})\|_*$

Input: $\mathbf{y}, h_0, \alpha, \gamma, \nu$

Initialization:
1: $X = \underset{X}{\arg\min}\frac{1}{2}\|RX - \mathbf{y}\|_Q^2$
2: $g_{t,e} = \alpha\frac{\|R^T Q_{t,e}\mathbf{y}\|_2}{\|\mathbf{x}_{t,e}\|_2}$
3: $V = 0$

While not converged...
4: $D = RSKR(X + V, h_0, \gamma, \nu)$
5: $V = V + X - D$
6: $X = \underset{X}{\arg\min}\frac{1}{2}\|RX - \mathbf{y}\|_Q^2 + \frac{G}{2}\|X + V - D\|_2^2$
End While

Input: $X + V, h_0, \gamma, \nu$

Initialization:
4a: $m_{e,e} = \mu_{water,e} * 1.4826 * MAD\left(\nabla\left(\frac{x_{:,e}+v_{:,e}}{\mu_{water,e}}\right)\right)$
4b: $[U_0, E_0, V_0] = SVD\left[(X + V)_{n_x n_t \times n_e}M^{-1}\right]$
4c: $h_i = h_0\left(e_{0;1,1}/e_{0;i,i}\right)^\gamma$
4d: $U = U_0, F = 0$

While not converged...
4e: $L = jBF(U + F)$
4f: $L = pSVT((L)_{n_x n_t \times n_t}, \nu)$
4g: $L = (L)_{n_x n_t \times n_e}$
4h: $F = U + F - L$
4i: $U = \underset{U}{\arg\min}\frac{1}{2}\|U - U_0\|_2^2 + \frac{h}{2}\|U + F - L\|_2^2$
End While

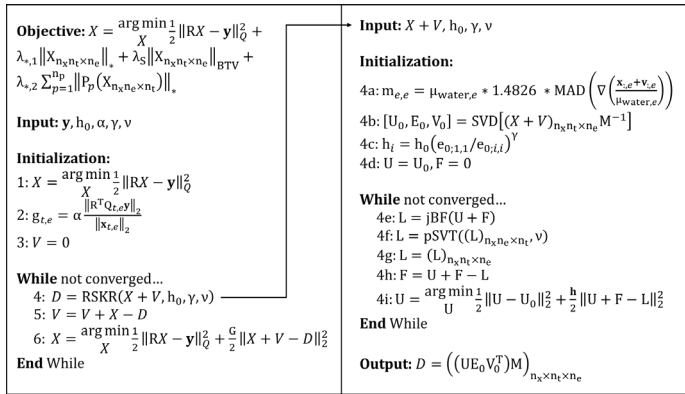**Output:** $D = \left((UE_0V_0^T)M\right)_{n_x n_t \times n_e}$

Fig. 1. The split Bregman method applied for iterative reconstruction of photon-counting CT perfusion data. Starting from the left column, an Initialization procedure estimates the reconstructed data, X, and the regularization parameters, G (here $\alpha = 0.007$, $h_0 = 1.5$, $\gamma = 0.5$, $\nu = 0.7$). Outer Bregman iterations approximately solve the Objective function through regularization (step 4, D), residual (5, V), and data fidelity (6, X) updates. More details on the inner Bregman iterations for regularization are provided in the text (steps 4a-4i). Six iterations of the Bi-CGSTAB(2) solver (algorithm 3.1 in [14]) are used to update X at each time point and energy during Initialization (step 1) and for each data fidelity update (step 6). Additional notation: $\mu_{water,e}$, the expected attenuation of water at energy threshold e; ∇, compute high-pass only component of the 3D Haar wavelet transform.; i, singular value, vector index (n_e total); $\mathbf{x}_{:,e} + \mathbf{v}_{:,e}$, time indices assumed equivalent for noise estimation.

2.3 Spectral processing and analysis

We compare three sets of reconstruction results: analytical reconstructions of each time point and energy (WFBP algorithm[15]), iterative reconstruction without pSVT (Fig. 1, steps 4f and 4g skipped), and iterative reconstruction with pSVT (Fig. 1, all steps). Notably, the reference iterative reconstruction (no pSVT) is similar to spectral reconstruction results we have quantitatively validated in previous work[7] (with the exception of localized noise estimation now performed during jBF). Following reconstruction, we perform non-negative material decomposition using sensitivity matrix inversion and a sub-space projection with iodine (red), photoelectric (PE, green), and Compton scattering (CS, gray) basis functions.[3] We characterize the convergence of our iterative reconstructions (Fig. 1, step 6) by measuring the relative error after the final outer Bregman iteration for each perfusion phase and energy threshold (generically, $\|A\mathbf{x} - \mathbf{b}\|_2/\|\mathbf{b}\|_2$; $A\mathbf{x}$: variable terms; $\mathbf{b}$: constant terms). We compare our reconstruction results through standard deviation measurements, residual images, material decomposition errors in reference solutions, and through modulation transfer function measurements.

2.4 Computation

All reconstruction and denoising operations were performed with our custom multi-channel GPU-based reconstruction toolkit.[16] For the mouse data set, a total of 6000 projections were acquired over 12, 360° rotations. The temporal basis functions (*rect* functions, $Q_{t,e}$) assigned equal weight to every projection in each subset of 500 projections, allowing reconstruction of 12 non-overlapping perfusion phases spanning 45 seconds each. Combined, 12 perfusion time points at 4 four energy thresholds were reconstructed (48 total volumes) with a volume size of 360x360x384 voxels and 125-micron, isotropic voxels. For the analytical reconstruction results, a ramp filter was used. For algebraic reconstruction (Fig. 1, steps 1 and 6) six iterations of the Bi-CGSTAB(2) solver were used.[14] Reconstructions were performed on an Ubuntu Linux workstation (v18.04) with four NVIDIA RTX8000 GPUs, 256 GB of system RAM, and two Intel Xeon W-2295 CPUs. Iterative reconstruction of all 48 volumes took 2.9 hours without pSVT (3 outer, 3 inner Bregman iterations) and 11 hours with pSVT (3 outer, 4 inner Bregman iterations).

3. RESULTS

Fig. 2 summarizes the perfusion reconstruction results along the energy dimension. Specifically, analytical WFBP, iterative reconstruction without pSVT, and iterative reconstruction with pSVT results are compared at perfusion phase 6. The final data fidelity update step of the outer Bregman iterations (Fig. 1, step 6) converged to within 4% error with pSVT and to within 3% error without pSVT for each individual energy threshold and perfusion phase, suggesting robust algorithm convergence. The noise standard deviation was measured in a water vial included in the scan. As expected, the noise level increases from 123 to 362 HU with increasing energy threshold (reduced photon counts). Our standard iterative reconstruction method (no pSVT), which includes data adaptation (Fig. 1, steps 2 and 4a), reduces the noise level by 2 to 7 times and equalizes the noise standard deviation across energy channels. Even with identical reconstruction hyperparameters (Fig. 1, "Input"), adding pSVT to the reconstruction further reduced noise by ~45%. Iterative reconstruction with and without pSVT yielded similar spatial resolution (20 keV energy threshold; 50% cutoff of the MTF: ~2.5 lp/mm in both cases).

Fig. 3 summarizes the reconstruction results along the prefusion dimension ("P6": perfusion phase 6), comparing the phase of minimum enhancement (phase 1) with phases of intermediate (2) and peak enhancement (6). The prefusion results are shown as material decomposition maps to emphasize the value of energy information in quantitatively separating soft tissue (CS), calcium (PE), and iodine (I). Additional CT images demonstrate the value of iterative reconstruction in enforcing redundancy between energy channels to counteract noise amplification associated with material decomposition and analytical reconstruction. Based on material calibration vials included in the scan (12 mg/mL I; 1.0 × water for PE, CS), material decomposition with and without pSVT yields similar mean material decomposition accuracy, but pSVT has lower noise (pSVT, no pSVT mean ± standard deviation: 11.67 ± 0.18, 12.08 ± 0.52 I; 0.68 ± 0.11, 0.68 ± 0.32 PE; 0.93 ± 0.03, 0.93 ± 0.08 CS). This is in stark contrast to the WFBP results, which are less accurate for I and CS, and have an order of magnitude larger standard deviations. Yellow arrows in Fig. 3 highlight an artifact pattern that is removed with the addition of pSVT; however, blue arrows point to a cervical lymph node metastases where the iodine map magnitude appears reduced when pSVT is added to the reconstruction. Further investigation is needed to characterize the trade-offs between spatial, spectral, and temporal resolution as a function of pSVT hyperparameters.

4. DISCUSSION AND CONCOLUSIONS

In this work, we have demonstrated the future of perfusion imaging with X-ray CT and PCD technology. Given the increases in noise associated with photon binning, data acquisition and hardware constraints, and spectral post-processing, a new class of algorithms will be required which take full advantage of the inherent structure in multi-channel CT data. We repurpose our existing multi-channel iterative reconstruction algorithm for compatibility with time- and energy-resolved perfusion data and propose a novel extension with pSVT. pSVT removes additional noise by exploiting data consistency along the temporal perfusion dimension.

The current work has several limitations. The imaging dose and contrast agent dose are non-trivial and unsuitable for longitudinal studies. Furthermore, the computation time associated with batched SVD operations for pSVT is too significant for routine use. In previous work,[17] we have demonstrated that similar challenges can be overcome for multi-channel cardiac CT reconstruction using deep learning. Extending this approach, we propose to use our current reconstruction algorithms and data acquisition protocol to generate high quality reference data. We could then artificially degrade these data sets and use a supervised learning paradigm to learn to map computationally inexpensive analytical reconstructions to our high-fidelity iterative reconstructions.
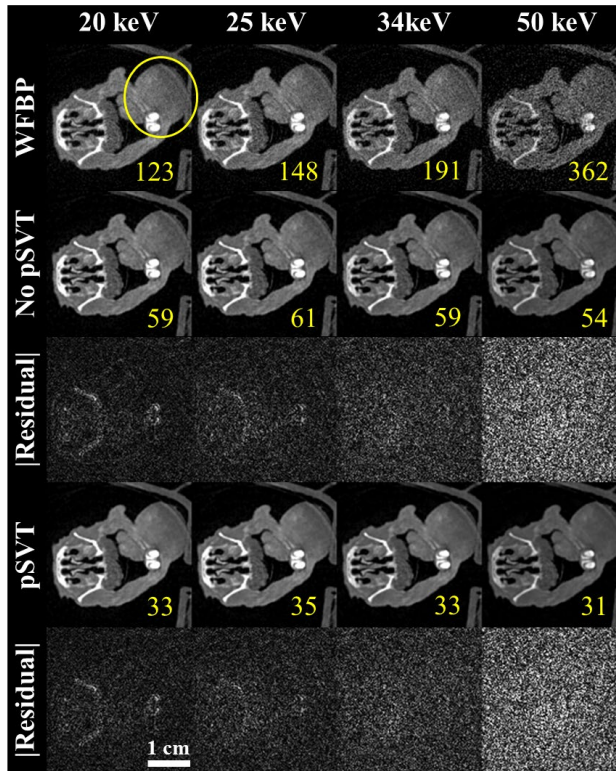
Fig. 2. Axial WFBP reconstruction results at perfusion phase 6 (row 1) are compared with matching iterative reconstruction results excluding ("No pSVT", row 2) and including ("pSVT", row 4) the pSVT regularizer. A yellow circle indicates the location of the primary tumor. Yellow text indicates noise standard deviation values measured in water for each energy threshold and reconstruction algorithm (HU; water vial not shown). CT window: [0.0,0.80] cm^{-1}. Absolute residual window: [0.0,0.16] cm^{-1}.
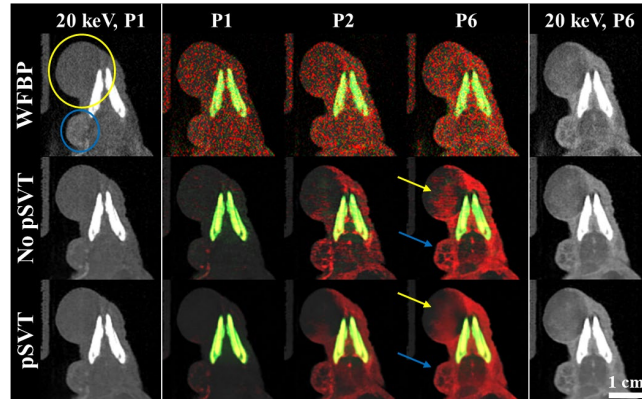
Fig. 3. Coronal CT images and material decomposition results are compared between WFBP reconstruction (row 1) and regularized iterative reconstruction excluding ("No pSVT", row 2) and including ("pSVT", row 3) pSVT. A yellow circle indicates the location of the primary tumor, while a blue circle indicates the location of a metastatic tumor. Results are shown for perfusion phases 1, 2, and 6 ("P6"). Arrows are referred to in the text. CT window: [0.0,0.80] cm^{-1}. Iodine (red) window: [1.0,6.0] mg/mL. PE (green) window: [1.0,15.0] × water. CS (gray) window: [0.0,8.0] × water.

5. ACKNOWLEDGEMENTS

REFERENCES

[1] M. J. Willemink, M. Persson, A. Pourmorteza, N. J. Pelc, and D. Fleischmann, "Photon-counting CT: technical principles and clinical prospects," Radiology 289(2), 293-312 (2018).

[2] R. Gutjahr, A. F. Halaweish, Z. Yu, S. Leng, L. Yu, Z. Li, S. M. Jorgensen, E. L. Ritman, S. Kappler, and C. H. McCollough, "Human Imaging With Photon Counting–Based Computed Tomography at Clinical Dose Levels: Contrast-to-Noise Ratio and Cadaver Studies," Investigative Radiology 51(7), 421-429 (2016).

[3] C. T. Badea, D. P. Clark, M. Holbrook, M. Srivastava, Y. Mowery, and K. B. Ghaghada, "Functional imaging of tumor vasculature using iodine and gadolinium-based nanoparticle contrast agents: a comparison of spectral micro-CT using energy integrating and photon counting detectors," Physics in medicine and biology (2019).

[4] J. R. Ashton, J. L. West, and C. T. Badea, "In vivo small animal micro-CT using nanoparticle contrast agents," Frontiers in pharmacology 6(256 (2015).

[5] H. Lewis-Jones, S. Colley, and D. Gibson, "Imaging in head and neck cancer: United Kingdom national multidisciplinary guidelines," The Journal of Laryngology & Otology 130(S2), S28-S31 (2016).

[6] N. P. Judd, A. E. Winkler, O. Murillo-Sauca, J. J. Brotman, J. H. Law, J. S. Lewis, G. P. Dunn, J. D. Bui, J. B. Sunwoo, and R. Uppaluri, "ERK1/2 regulation of CD44 modulates oral cancer aggressiveness," Cancer research 72(1), 365-374 (2012).

[7] D. P. Clark, and C. T. Badea, "Hybrid spectral CT reconstruction," PLOS ONE 12(7), e0180324 (2017).

[8] D. Clark, M. Holbrook, C. Lee, and C. Badea, "Photon-counting cine-cardiac CT in the mouse," PLoS ONE 14(9), e0218417 (2019).

[9] K. Kim, J. C. Ye, W. Worstell, J. Ouyang, Y. Rakvongthai, G. El Fakhri, and Q. Li, "Sparse-view spectral CT reconstruction using spectral patch-based low-rank penalty," IEEE Transactions on Medical Imaging 34(3), 748-760 (2015).

[10] H. Gao, H. Yu, S. Osher, and G. Wang, "Multi-energy CT based on a prior rank, intensity and sparsity model (PRISM)," Inverse Problems 27(11), 115012 (2011).

[11] E. J. Candès, X. Li, Y. Ma, and J. Wright, "Robust principal component analysis?," Journal of the ACM (JACM) 58(3), 11 (2011).

[12] D. L. Donoho, and I. M. Johnstone, "Adapting to unknown smoothness via wavelet shrinkage," Journal of the American Statistical Association 90(432), 1200-1224 (1995).

[13] D. P. Clark, and C. T. Badea, "Spectral diffusion: an algorithm for robust material decomposition of spectral CT data," Physics in Medicine and Biology 59(21), 6445 (2014).

[14] G. L. Sleijpen, and M. B. Van Gijzen, "Exploiting BiCGstab (ℓ) strategies to induce dimension reduction," SIAM journal on scientific computing 32(5), 2687-2709 (2010).

[15] K. Stierstorfer, A. Rauscher, J. Boese, H. Bruder, S. Schaller, and T. Flohr, "Weighted FBP—a simple approximate 3D FBP algorithm for multislice spiral CT with good dose usage for arbitrary pitch," Physics in Medicine & Biology 49(11), 2209 (2004).

[16] D. P. Clark, and C. T. Badea, "GPU-Based Tools for Multi-Channel X-ray CT Reconstruction," F. Noo, Ed., *The Fifth International Conference on Image Formation in X-Ray Computed Tomography* (2018).

[17] D. P. Clark, and C. T. Badea, "Convolutional regularization methods for 4D, x-ray CT reconstruction," in *Proceedings of SPIE Medical Imaging*, pp. 1-12. (2019 Paper #10948-81).